Journal of Power Sources 206 (2012) 84–90

Contents lists available at SciVerse ScienceDirect

Journal of Power Sources

journal homepage: www.elsevier.com/locate/jpowsour

Experimental study of single triple-phase-boundary and platinum–yttria stabilized zirconia composite as cathodes for micro-solid oxide fuel cells

Yan Yan*, Silviu Cosmin Sandu, Janine Conde, Paul Muralt

Ceramics Laboratory, Ecole Polytechnique Fédérale de Lausanne (EPFL), Lausanne CH-1015, Switzerland

ARTICLE INFO

Article history:
Received 9 December 2011
Received in revised form 13 January 2012
Accepted 17 January 2012
Available online 25 January 2012

Keywords:
Micro-solid oxide fuel cell
Triple phase boundary (TPB)
Pt–YSZ composite
Cathode
Thin film

ABSTRACT

Micro-solid oxide fuel cell (μSOFC) structures with annular Pt electrodes have been fabricated by means of silicon micromachining. The annular cathodes contained a defined triple phase boundary (TPB) length, which allowed the derivation of the ionic current per length of TPB as 1.24 mA m^{-1}, measured at 450 °C at maximal power. Considering literature values for oxygen diffusion activation on Pt, the active zone supplying atomic oxygen to the triple phase boundary was calculated to be 22 nm wide at most. The anode function was provided by a CGO layer, known to be electrically conductive at reducing conditions, with annular Pt current collector. The TPB length was increased by adding a Pt–YSZ composite cathode layer covering the complete YSZ/CGO membrane. The peak power density was increased by a factor of 5 to reach 5 mW cm^{-2} with an open circuit voltage of 0.68 V at 450 °C. It was observed that the Pt grains re-crystallized to large grains, leading to a loss of electrical connectivity in the composite layer. The composite cathode layer was thus inadequate to contact the complete membrane area, leading to a too large area specific resistance (ASR) in the interior of the cell.

1. Introduction

Low temperature solid oxide fuel cells (SOFCs), operating under 550 °C, are considered to be effective solutions for power supplies of portable electronic devices with high consumption, and electric vehicles [1]. The small-scale SOFCs, referred to as micro-SOFCs (μSOFCs) fabricated by micro-machining and thin film technology achieve such low operation temperatures, and therefore have great promises as portable power sources for devices such as mobile phones, digital cameras, laptops, etc. [2–4]. Low temperature operation results in increased resistances from the electrolyte and electrodes [5,6] as compared to classical SOFC operation conditions. The limitation of ion transport through the electrolyte can be removed by reducing its thickness. However, a general agreement exists that the overall performance of μSOFCs is limited by oxygen reduction reactions (ORR) on the cathode [7,8]. In existing high-temperature SOFC's the cathode typically consists of porous layers of mixed electronic/ionic oxides such as $(La,Sr)(Co,Fe)O_3$ [9].

Platinum was employed as a routine electrode material for low temperature SOFC's considering the impressive performance below 500 °C [10,11]. It was shown that the ORR process takes place at the triple phase boundary (TPB) lines formed by the metal phase, the electrolyte phase and the gas phase [8,12,13]. In the case of a pure electron conductor like Pt, the sequence of events going on is sketched in Fig. 1. Molecular oxygen is adsorbed and dissociated (1) on the Pt cathode. The atomic oxygen diffuses (2) to the TPB, and is caught by an oxygen vacancy in the electrolyte of yttria stabilized zirconia (YSZ) together with two electrons (3). In the past, it was also considered that the reaction might go on at the Pt/YSZ interface but this did not fit to experimental findings [13]. The width of the TPB is thus composed of the diffusion region on the electrode, and of a narrow region on the YSZ surface that is reached by electrons and atomic oxygen to occupy a vacancy. All the ionic current must pass through this constricted region. Its width or depth was estimated to be around 10 nm [14].

A number of research works investigated the kinetics of the $Pt(O_2)$/YSZ system to clarify the reaction mechanism and the rate-limiting step of the ORR [8,12,13,15,16]. It has been recently confirmed that the rate-limiting step is located close to the TPB by studying electrodes of different sizes indicating that the impedance evolution scaled well with the circumference of the Pt electrodes, but not with the area of the electrodes [16]. However, no work has been done to evaluate the current density or power density per TPB length for a working SOFC device. In most cases the TPB length was unknown because an undefined porous cathode was used, or the works were restricted to impedance studies. A number of modeling studies were devoted to kinetic issues of mixed conducting electrodes [7,17]. For the Pt cathodes it was concluded

* Corresponding author.
E-mail address: yan.yan@epfl.ch (Y. Yan).

0378-7753/$ – see front matter © 2012 Elsevier B.V. All rights reserved.
doi:10.1016/j.jpowsour.2012.01.113

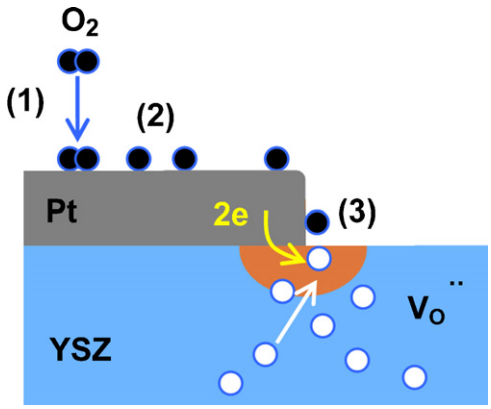

Fig. 1. Reaction scheme for oxygen reduction process of Pt/YSZ system. (1) O_2(g) adsorption; (2) O_2 dissociation; (3) atomic oxygen diffusion on the Pt surface; (4) oxygen reduction with electron capture at the TPB, yielding O^{2-} capture by vacancy site.

that a narrow, 50–500 nm wide, active region on Pt close to the TPB line is providing oxygen adsorption and supply to the TPB [8]. In a modeling study, this active region was estimated to be 10 nm wide (T = 975 and 1071 K) [18]. In a study of impedance modeling of TPB's Pt/YSZ another scale issue was considered, namely the width of the TPB within the YSZ (or rather the hemi-cylindrical region through which the current has to reach the edge of the Pt electrode) [14]. The TPB width affected the corresponding dependence of electrolyte resistance on the thickness. However, a more complex model was needed to derive an estimated TPB width from the constriction resistance derived from electrical impedance spectroscopy (EIS) [14].

Optimal electrode systems exhibit a large total length of TPB's, either by applying porous electrodes [19–21], or by introducing a more complex electrode/electrolyte nano-composite, which in theory should have an even larger TPB total length [11,22,23]. To date, most of the results concern large planar SOFCs working at high temperatures. The major problems of nano-composites are the thermal instability of their microstructure, or even their chemical incompatibility [8,24–27]. For μSOFC's nano-porous microstructures are required to distribute well the current with the electrolyte. However, the results demonstrated so far do not show reliable and repeatable performance in case of μSOFC's cells with their submicron thick electrolyte membranes. Therefore, the composite cathodes of μSOFCs remain a challenge. Hertz et al. [23] fabricated co-sputtered nano-composites with area specific resistances (ASR) of less than 500 Ω cm^2 at 400 °C, however, no power density was reported.

In this work, we designed and fabricated Pt/CGO/YSZ/Pt cells with a geometrically well-defined TPB circle at the outer side of the membrane. This construction serves to two purposes. It allows firstly for measuring the current or power density per TPB length, and secondly it allows for contacting the composite material deposited as the last process step for our μSOFC. A top view of the membrane array is shown in Fig. 2(a). A single cell is situated in the crossing of a vertical and a horizontal conductor line. With 8 lines each, we obtain 64 cells on one chip.

2. Experimental

2.1. YSZ/CGO electrolyte

Deposition of 8 mol% YSZ electrolyte thin films was performed by an RF magnetron sputtering system (Nordiko 2000) in 5 mTorr argon atmosphere at a substrate chuck temperature of 500 °C. The RF power was fixed at 200 W, corresponding to a power density

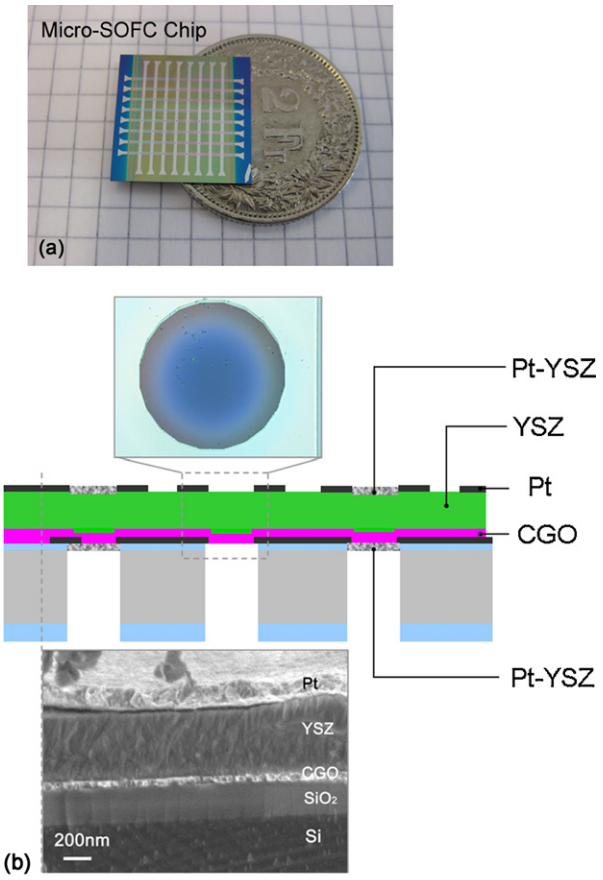

Fig. 2. μSOFCs' devices: (a) a top view photograph of 64 free-standing membrane matrix on a silicon chip. For each cross there is a 200 μm diameter membrane. (b) Cross sectional view of fabricated μSOFCs' components and design. The insert show a top view of an individual membrane with the annular Pt electrode at the outer zone, as obtained after the back-side dry etching step and cross section of a Pt/YSZ/CGO membrane on the edge of the SiO_2/Si substrate.

of 2.5 W cm^{-2}. The ceramic target contained 99.9% pure zirconia doped with 8 mol% yttria (Kurt J. Lesker). Gadolinium doped ceria ($Ce_{0.8}Gd_{0.2}O_2$) thin films were sputtered from a metallic target made of a cerium gadolinium alloy, which contained 13 at% Gd. The chamber was evacuated to a base pressure of less than 2×10^{-6} Torr before starting the process. The process parameters were the same as for YSZ, except that the RF power amounted to 150 W, and the sputter gas was a 1:1 mixture of argon and oxygen. After deposition, all the samples of YSZ and CGO were cooled down in 80 mTorr of pure oxygen. The experimental setup and parameters have been described in detail elsewhere [28,29].

2.2. Pt–YSZ composite

The Pt–YSZ composite thin films were deposited by dynamic, parallel sputtering onto a rotating substrate holder, the substrate passing periodically above the Pt and YSZ cathodes. The rotation speed amounted to 6 rpm. The composite films were deposited at room temperature in an argon/oxygen atmosphere. Further parameters are given in Table 1. The conditions were chosen to reach about a 50:50 composition.

2.3. Cell fabrication

In our design of μSOFCs arrays, the 200 μm diameter free-standing membranes are fabricated on SiO_2-coated silicon wafers, before dicing into1.8 cm × 1.8 cm chips as shown in Fig. 2(b). The Pt

Table 1
Deposition conditions for Pt–YSZ composite thin films.

Pt–YSZ composite thin film	Pt target DC power (W)	YSZ target RF power (W)	Pressure (mTorr)	Deposition temperature (°C)	O_2/Ar gas ratio	Thickness (nm)
1	5	150	10	500	0.1	50
2	10	150	10	500	0.1	60

electrode stripes contain an opening of 160 μm diameter on each side of each membrane, thus forming a 20 μm wide Pt ring at the border of the membranes. New concept serves to improve the flexibility and diversity for cell optimization with various electrode layers. The process flow includes the following steps: (1) pattern the electrical insulating SiO_2 layers on the bottom side of the Si wafer to define the pattern liberating the membranes; (2) sputter deposition and patterning of the Pt film forming the anode current collector by dry etching; (3) sputter deposition of the YSZ/CGO electrolyte layer stack; (4) sputter deposition and dry etching of the Pt film forming the cathode current collector; (5) deep silicon back-side dry etching to free the membranes, whereby the etching stops on the oxide film; (6) removal of the oxide below the electrolyte and Pt ring by dry etching in CF_4; (7) dicing. The eventual co-sputter deposition of Pt–YSZ composite electrodes is performed dice per dice, and does not need a further patterning step. The chosen process route is a simplified version of the more complex fabrication of nickel-grid supported membranes described earlier [28].

2.4. Characterization

Film orientation and crystalline quality were examined by X-ray diffraction on a Bruker D8 Advanced X-ray diffractometer (Bruker AXS GmbH) using Cu Kα radiation. Surface morphology of thin films deposited on substrates was examined with a Zeiss LEO 1550 scanning electron microscope (SEM). Transmission electron microscopy (TEM) studies were performed on Pt–YSZ cross-sectional TEM specimens using a Philips FEI CM300 electron microscope at 300 kV. Film stresses were determined by wafer bow measurements of Tencor FLX-2900 system utilizing the Stoney relationship. All the samples deposited on silicon (1 0 0) substrates were measured prior to and after thin film deposition in air with the heating and cooling rates of 3.5 °C min^{-1} and holding at 600 °C for 1 h. The silicon substrates had a thickness of 540 μm, and biaxial modulus of 181 GPa was used for the stress calculation. For the electrochemical characterization of Pt–YSZ composite cathodes, post-annealing in air was performed in a Lenton 4793 tube furnace at 500 °C for 10 h. The ramping and cooling rates were both 5 °C min^{-1}. Higher temperature was not chosen considering fuel cell operation temperature, the subsequent micro-fabrication and integrated package. Impedance spectra were collected by a HP 4282 frequency response analyzer over a frequency range from 20 to 1 MHz with an AC voltage amplitude of 20 mV and zero DC bias in the temperature range of 280–500 °C in air. The details of cross-plane configuration can be found elsewhere [7,28,30]. *ZView* demo software was used to construct the equivalent circuit, perform the fitting and extract resistance and capacitance values.

The μSOFC performance was measured with a set up supplying a (25% H_2/75% Ar) gas flow to the anode side, and being open to air on the cathode side. This set-up can be placed on a hot chuck. The temperature was measured by a thermocouple placed on the μSOFC chip. The current from the anode to the cathode was collected by Pt needles placed on the two conductor lines defining the μSOFC element. The μSOFCs were activated in a reducing atmosphere on the anode side at 450 °C for 1 h at a heating rate of 2 °C min^{-1}.

3. Results and discussion

3.1. Single TPB cells with annular Pt electrodes

Fig. 3 shows the microstructure of the edge of annular Pt ring on top of the YSZ membrane in a μSOFC chip annealed in ambient air for 10 h at 450 °C. The Pt thin film peels off at the very beginning of the edge, giving rise to a roughly 200 nm wide belt containing larger grains after annealing. Further away from the border, good adhesion is maintained with a practically unchanged film morphology. At 450 °C, the TPB is thus rather well defined by a circle of 160 μm radius. This temperature does not yet lead to a meandering shape. The $V(I)$ characteristic of such a cell can thus be ascribed to a known TPB length on the cathode side. The anode function is provided by the reduced CGO film and annular Pt current collector present on the anode side. At 450 °C, an open circuit voltage (OCV) of 0.97 V was measured seen in Fig. 4. The voltage shows the expected linear decrease with increasing current density. The maximal power density is derived as 1.25 mW cm^{-2}, if we consider the complete membrane area (inner part with no electrode, i.e. circular area with 80 μm radius). For a predicted OCV by Nernst equation, it is important that all membranes on a chip are intact. Otherwise air leakage through the broken membrane leads to a larger oxygen pressure on the anode side. The $V(I)$ curve of such a situation is also shown in Fig. 4. The OCV decreased to 0.47 V while the peak power density dropped to 0.50 mW cm^{-2}.

The CGO layer on the anode side is sufficiently reduced by the fuel to act as electronic and ionic conductor at the same time. Electronic conduction in reduced CGO was studied in Ref. [31]. The electronic specific conductivity was determined to be 4.5 Sm^{-1} at 700 °C with and activation energy of 0.73 eV [31]. Form these data, one calculates a conductivity of 0.22 Sm^{-1} at 450 °C. Assuming that the current spreads to a width 100 μm on the anode side, the voltage loss in CGO amounts to 0.6 mV, and is thus negligible as compared to the cathode polarization. We thus can infer that the circular TPB line limits the current (which is confirmed later by adding more cathode electrode area). This allows for measuring

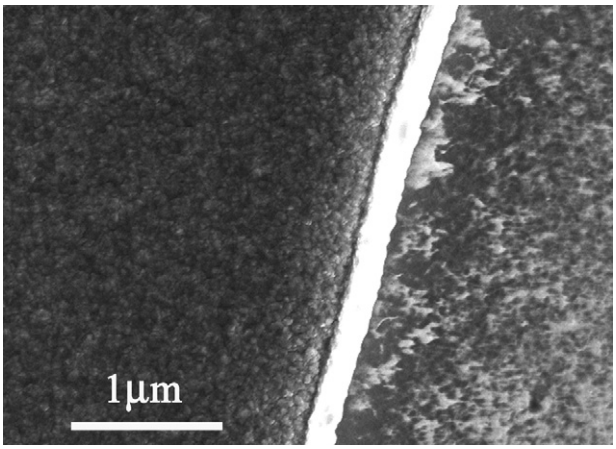

Fig. 3. SEM top-view image showing the border region of the annular Pt electrode (left) on top of the YSZ membrane (right) after annealing in ambient air at 450 °C for 10 h. The white ribbon is the Pt film that peeled off on the last micrometer from its border and was reshaped during anneal.

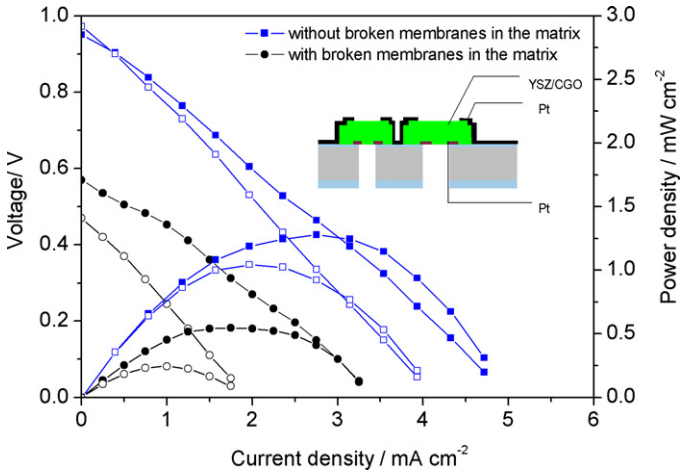

Fig. 4. Voltage and power density as a function of the average current density of μSOFCs at 400 °C (open symbols) and 450 °C (solid symbols), exhibiting a Pt cathode covering only the border of the membrane. Broken membranes in the matrix lead to oxygen leaking to the anode side, thus reducing the voltage. The anode consists of a CGO film, contacted at the border of the membrane by a Pt layer.

the current density per TBL length at a particular temperature and oxygen pressure. In Fig. 4, the maximal power density at 450 °C corresponds to a current density per TPB length of $j_e = 1.2\,\mathrm{mA\,m^{-1}}$. A corresponding flux of oxygen atoms must be supplied from the Pt electrode. There is a certain "active" region adjacent to the TPB that has the role to adsorb oxygen gas, dissociate into oxygen atoms, and provide oxygen diffusion to the TPB. The kinetic rate model is similar to those derived for adsorption [15]. This supply is either limited by the dissociation rate of adsorbed molecular oxygen (Langmuir isotherm), or the diffusion process [15]. It was found that there is a crossover from limiting diffusion to limiting dissociation at about 500 °C. At 450 °C, we are thus close to this limit, but still in the diffusion limited case. The diffusion flux depends on the density of oxygen atoms on the surface, which is installed at equilibrium according to the dissociation reaction:

$$O_{2(g)} + 2V_{ad}(\mathrm{Pt}) \rightarrow 2O_{ad}(\mathrm{Pt}) \tag{1}$$

The reaction constant can be written as $K(T) = K_0 \exp(-H_{ad}/kT)$, where H_{ad} is the activation energy for the combined dissociation–adsorption. By introducing the occupancy factor $\theta = \mathrm{O_{ad}/N_{ad}}$, $1-\theta = V_{ad}/N_{ad}$, where N_{ad} is the density of adsorption sites (roughly one per Pt atom on the surface), O_{ad} the density of occupied sited, and V_{ad} the density of empty sites, the reaction equation becomes:

$$\frac{\theta}{1-\theta} = (p_{O_2} K(T))^{1/2} \tag{2}$$

The equilibrium oxygen pressure $p^*_{O_2}$ at which the occupancy amounts to 0.5 yields the reaction constant at infinite temperature K_0: $K_0 = (p^*_{O_2})^{-1} \cdot \exp(H_{ad}/kT)$. The occupancy ratio is obtained from the $p^*_{O_2}$ as

$$\frac{\theta}{1-\theta} = \left(\frac{p_{O_2}}{p^*_{O_2}}\right)^{1/2} \tag{3}$$

At 400 °C and 450 °C, $p^*_{O_2}$ amounts to 3.2×10^{-6} and 3.2×10^{-7} atm extracted from [12]. As we are working at 200 mbar O_2, we obtain a practical complete occupancy with atomic oxygen $\theta_0 = 0.99$ in this temperature range.

Considering a pure stochastic motion of atomic oxygen, there is an ordinary diffusion going on, yielding an oxygen flow density j_O according to the concentration gradient, in this case of the empty adsorption sites.

$$j_O = -j_V = D \cdot \nabla(1-\theta) N_{ad} = -D N_{ad} \cdot \nabla\theta \tag{4}$$

We consider a distance between adsorption sites of a_{ad}. The density of adsorption sites has thus a value of $N_{ad} = a^{-2}$. D_0 is obtained from standard arguments for ad-atom hopping at infinite temperature, at which the adatom jumps to the next place (at distance a_{ad}) at the pace of the inverse hopping attempt rate ν. As the distance goes with the square of the time, D_0 is obtained as:

$$D_0 = \frac{1}{b} \nu a_{ad}^2 \tag{5}$$

where b is the degree of freedom for the hopping direction. For the present estimation we use the value for D_0 as given in [32] and assume a hopping distance of 2.8 Å equal to the periodicity of a Pt(1 1 1) surface. The attempt rate in a given direction is then obtained as $\nu/b = 1.3 \times 10^{12}$ Hz, which corresponds as expected to optical phonon frequencies. From literature [32] we know that the diffusion activation energy E_d amounts to 0.6 eV:

$$D = D_0 \exp\left(-\frac{E_a}{kT}\right) \tag{6}$$

The atomic oxygen flux density j_O is then obtained as:

$$j_O = D N_{ad} \cdot \nabla\theta \approx \frac{\nu}{b} \exp\left(-\frac{E_a}{kT}\right) \frac{\theta_0}{\lambda} \tag{7}$$

For the gradient, we assume that within the active region of width λ, the oxygen occupancy drops from equilibrium value θ_0 far away from the TPB to zero at the TPB. As each oxygen atom is accompanied by two electrons (each having unit charge e) from the electrode, λ is then obtained from the electrical current density j_e as:

$$\lambda \approx -\frac{2\nu\theta_0 e}{b j_e} \exp\left(-\frac{E_a}{kT}\right) \tag{8}$$

Eq. (8) yields a λ of 22 nm. This length can be considered as an upper value for the TPB width on the Pt electrode side at 450 °C. This value is larger than the estimation of 10 nm at 602 °C as given in [18]. This value cannot be compared directly with TPB widths of mixed oxide conductors, such as LSCF for which a TPB width of 1.39 μm was derived for $T = 950$ °C [17]. Nevertheless, assuming a diffusion activation energy of 0.5 eV, this width would shrink to 50 nm at 450 °C.

We can now propose an ideal geometry for Pt based cathodes. In order to achieve 1 A cm^{-2} current density at 450 °C, a Pt grid with a cell side length of about 100 nm is needed based on the measured current density per TPB line. The estimated width of the active TPB is compatible with such an approach. Nanograined, porous Pt thin films look ideal to achieve such kind of a structure. However, nanograined Pt films are not stable and recombine into larger meander patterns [8,11], the electrical resistance is increased, and the TPB length is reduced. Porous Pt recrystallizes and is de-wetting from the surface of a YSZ electrolyte layer, as shown in Fig. 5 for a film annealed at 500 °C for 2 h in air. The segregation of Pt induces a significant performance degradation and is a function of cell operational temperature, time and environment [11,33]. We studied the concept of Pt–YSZ composite films, hoping that recrystallization and dewetting are reduced by the co-sputtered YSZ phase.

3.2. Characterization and electrochemical performance of Pt–YSZ composite films

The film microstructure and morphology change dramatically during annealing at 500 °C, as shown in Fig. 6. While we deal with a smooth, nano-structured film before in the as-deposited state, the

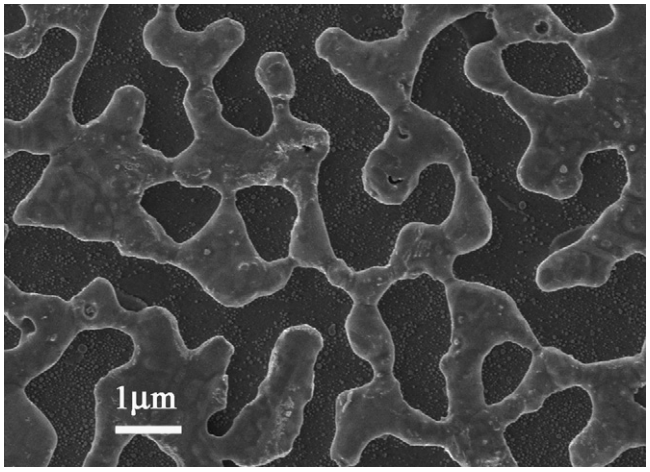

Fig. 5. SEM image of 100 nm sputtered, nanograined platinum thin film on top of the YSZ electrolyte after cell operation at 550 °C in fuel gas for 2 h.

annealed film exhibits large Pt grains above a matrix of YSZ mixed with smaller Pt grains. It is evident that the composite structure does not escape from segregation processes, even though the two phases were mixed on the nanometer level after deposition. Clearly, YSZ in the room temperature co-sputtered composite cannot stabilize the Pt phase effectively.

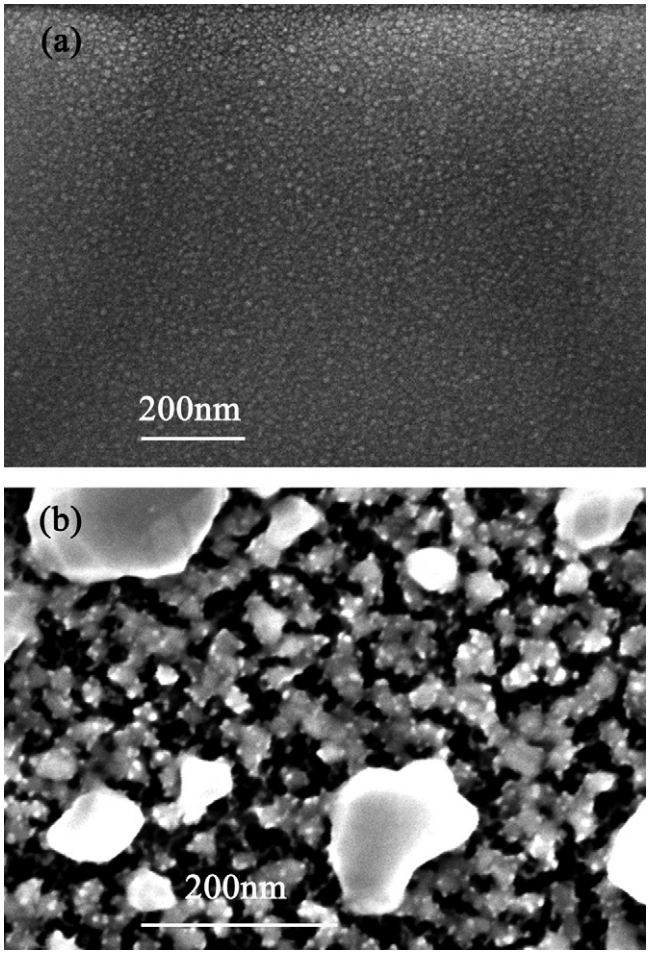

Fig. 6. SEM images of the 5/150 W sample before (a) and after annealing at 500 °C (b).

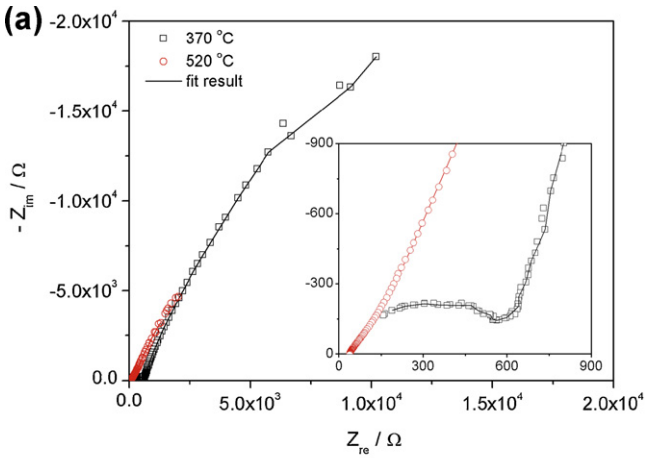

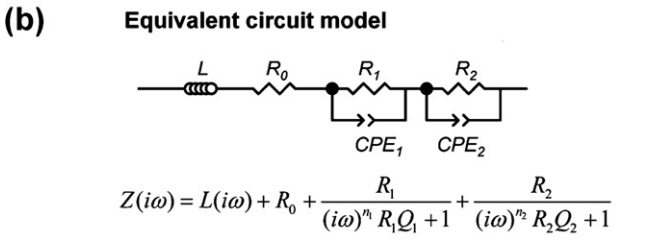

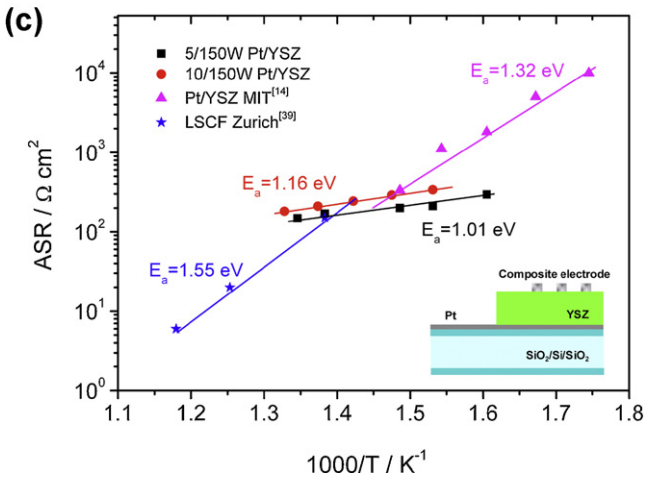

Fig. 7. (a) Impedance spectra (Cole–Cole plots) measured on 400 μm composite electrodes at 370 °C and 450 °C. The insert shows the high frequency part of the spectra. (b) Equivalent circuit model used for the complex fits. (c) The area specific resistance (ASR) of the Pt–YSZ composite cathode layers on YSZ/Pt substrate exposed to air atmosphere.

Fig. 7(a) shows impedance spectra (Cole–Cole plots) of Pt–YSZ/YSZ/Pt stacks with the composite electrode on top at different operating temperatures. The curves consist of two depressed arcs, a small or a shoulder one appearing at high frequencies and a huge one in low frequency range. There is no difference for the two composite electrodes with nominally each identical composition. The data in this paper were fitted with the equivalent circuit model as shown in Fig. 7(b). Various equivalent circuits have been used in the literature to model the complex impedance spectra of composite films [23,34]. In the equivalent circuit, R_0 is assigned to the ohmic resistance from connection wires in the measuring system. CPE_1 and CPE_2, in parallel with the ohmic resistance R_1 and R_2, represent the constant phase elements of high- and low-frequency arcs. Q and n are the pre-factor and the exponent of the CPE, respectively. The first semi-circle at high frequencies is expected to represent the resistance of the YSZ electrolyte [23] and the

one of low frequencies electrode processes. All types of resistance decreased with increasing temperature. The activation energy of 1.13 eV calculated from an Arrhenius plot of R_1 (dominated by ionic conduction through YSZ) as a function of the reciprocal temperature (not shown here) agrees well with the activation energies between 0.96 eV and 1.2 eV reported in the literature for the oxygen vacancy conduction in YSZ [35–37]. In earlier studies [23,38], composite electrode characteristics were found to depend on the microstructure related TPB length, which is often found to be the dominant contributor to the conductivity. It is assumed that the limiting steps is oxygen dissociative adsorption and oxygen atom surface transfer to the triple phase boundary, as for the oxygen exchange mechanisms of well defined Pt electrodes, or oxygen gas and ion diffusion within the YSZ phase of the composite structure. In this study, not all the conduction limiting mechanisms are simultaneously represented in the impedance spectra, thus no precise conclusion can be made concerning geometrical properties such as surface area or TPB-length. The very fine-grained porous microstructure would suggest that the current density is homogenous on the level of an area with diameter of the electrolyte thickness.

The R_1 value derived from impedance spectroscopy was multiplied with the electrode area for obtaining the area specific resistance (ASR) shown in Fig. 7(c) for the samples with 5/150 W and 10/150 W Pt–YSZ composite electrodes on an YSZ/Pt/SiO_2 layer stack. On the same graph, literature data for single-phase LSCF and porous composite electrodes on the YSZ surface [23,39] are shown for comparison. Our Pt–YSZ composites show smaller activation energies. We can interpret this as being the result of limitation by conduction within the electrode, or within the YSZ, and not by dissociation, or diffusion of oxygen. The low value close to 1.0 eV indicates ionic conduction through the YSZ phase, at least for the case of AC current. For DC current, the resistance at room temperature was measured to be very high within the electrode. The activation energies of 5/150 W and 10/150 W Pt–YSZ composite electrodes were measured as 1.01 eV and 1.16 eV, respectively. The change in the activation energy of the cathodic process with electrode composition may indicate a change in TPB length. In the low temperature range, the ASR of our samples is lower than the ones reported in the MIT study. This difference can be explained by the large difference in microsturcture of the composite films.

A 50 nm thick composite cathode layer of 5/150 W Pt–YSZ composite was deposited onto existing cells with ring electrodes. They were tested in the same way as the ring electrode cells on a stage exposing the anode side to a Ar/H_2 mixture. The generated current density is considerably increased, i.e. by a factor 5, as compared to the Pt ring version shown in Fig. 8. The open-circuit voltage was obtained as 0.68 V and the maximum power density as 4.22 mW cm^{-2} at a current density of 15 mA cm^{-2}. This means that the ASR is considerably reduced by Pt segregation leading to badly interconnected metallic conduction. The performance increases with electrode thickness, but less than proportional. The high temperature and long time annealing promote Pt diffusion, and hillock growth. It is thus rather the electrical conduction within the electrode than a polarization at the electrolyte/cathode interface [40] that limits performance. The OCV increases from 400 to 450 °C in all measured samples. This was also observed in previous works. In general, the OCV increases steeply somewhere below 400 °C and reaches a stable value at a certain temperature above or around 400 °C [41]. The electronic current leakage through the YSZ/CGO electrolyte is most likely responsible for the lower apparent OCV at low temperatures. The same arguments are also advanced in Ref. [42]. The addition of a Pt–YSZ composite anode did not improve the power density. This means that the CGO layer as mixed conductor together with annular Pt current collector on the anode side did not limit the current density, and that we observe cathode limitations

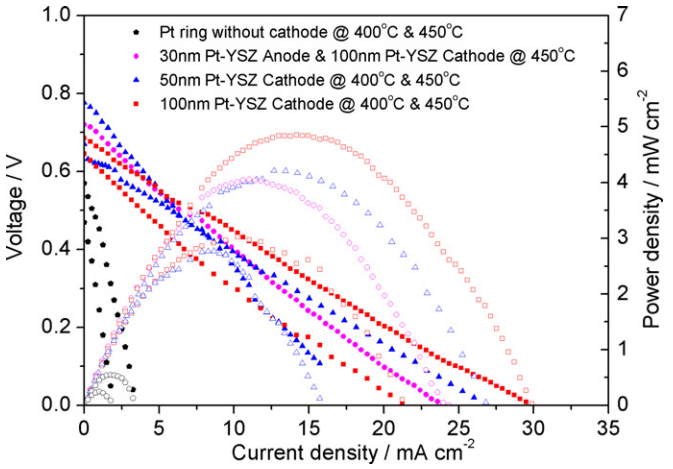

Fig. 8. Cell voltage vs. current density of cells on which a composite Pt–YSZ cathode layer was deposited (matrix with partially broken membranes).

only. Nevertheless, for high current densities, the Ni–CGO composite films as anodes show larger electronic conductivities than pure CGO layers, and should be considered in future.

4. Conclusion

The design of single Pt TPB of micro-SOFC directly links the predictions from modeling-based calculations with cell performances as measured in the test cells. The width of TPB for the Pt(O_2)/YSZ system is at most 22 nm wide at 450 °C. The cells show a limitation in electrode conduction. The maximum powder density of 4.82 mW cm^{-2} is observed for 100 nm Pt–YSZ composite/YSZ/Pt μSOFCs at 450 °C. The performance degradation is attributed to the Pt de-wetting as a function of operating temperature in the composite. We conclude that Pt–YSZ composite films are not ideal for low-temperature μSOFCs, in spite of the low operation temperature.

Acknowledgments

The authors acknowledge the financial support of ONEBAT project from Swisselectric Research, Swiss Competence Center on Energy and Mobility (CCEM), and Swiss National Science Foundation (CRSI22_126830/1).

References

[1] B.C.H. Steele, A. Heinzel, Nature 414 (2001) 345–352.
[2] J.P.H.A.F. Jankowski, R.T. Graff, J.D. Morse, Mater. Res. Soc. Symp. Proc. 730 (2002) 93–98.
[3] K. Nikbin, A. Nyilas, K. Weiss, AIP Conf. Proc. 824 (2006) 283–290.
[4] A. Bieberle-Hutter, D. Beckel, A. Infortuna, U.P. Muecke, J.L.M. Rupp, L.J. Gauckler, S. Rey-Mermet, P. Muralt, N.R. Bieri, N. Hotz, M.J. Stutz, D. Poulikakos, P. Heeb, P. Muller, A. Bernard, R. Gmur, T. Hocker, J. Power Sources 177 (2008) 123–130.
[5] Y.L. Liu, C.G. Jiao, Solid State Ionics 176 (2005) 435–442.
[6] S.P. Simner, M.D. Anderson, M.H. Engelhard, J.W. Stevenson, Electrochem. Solid State 9 (2006) A478–A481.
[7] J. Fleig, Annu. Rev. Mater. Res. 33 (2003) 361–382.
[8] S.B. Adler, Chem. Rev. 104 (2004) 4791–4843.
[9] L.W. Tai, M.M. Nasrallah, H.U. Anderson, D.M. Sparlin, S.R. Sehlin, Solid State Ionics 76 (1995) 259–271.
[10] H. Huang, M. Nakamura, P.C. Su, R. Fasching, Y. Saito, F.B. Prinz, J. Electrochem. Soc. 154 (2007) B20–B24.
[11] K. Kerman, B.K. Lai, S. Ramanathan, J. Power Sources 196 (2011) 2608–2614.
[12] J. Mizusaki, K. Amano, S. Yamauchi, K. Fueki, Solid State Ionics 22 (1987) 323–330.
[13] N.L. Robertson, J.N. Michaels, J. Electrochem. Soc. 137 (1990) 129–135.
[14] J.L. Hertz, H.L. Tuller, Solid State Ionics 178 (2007) 915–923.
[15] J. Mizusaki, K. Amano, S. Yamauchi, K. Fueki, Solid State Ionics 22 (1987) 313–322.

[16] A.K. Opitz, J. Fleig, Solid State Ionics 181 (2010) 684–693.
[17] J.D. Fehribach, R. O'Hayre, SIAM J. Appl. Math. 70 (2009) 510–530.
[18] A. Mitterdorfer, L.J. Gauckler, Solid State Ionics 117 (1999) 187–202.
[19] Y. Ohno, S. Nagata, H. Sato, Solid State Ionics 3–4 (1981) 439–442.
[20] V. Dusastre, J.A. Kilner, Solid State Ionics 126 (1999) 163–174.
[21] T. Suzuki, M. Awano, P. Jasinski, V. Petrovsky, H.U. Anderson, Solid State Ionics 177 (2006) 2071–2074.
[22] S. Bredikhin, G. Abrosimova, A. Aronin, K. Hamamoto, Y. Fujishiro, S. Katayama, M. Awano, J. Electrochem. Soc. 151 (2004) J95–J99.
[23] J.L. Hertz, H.L. Tuller, J. Electrochem. Soc. 154 (2007) B413–B418.
[24] M.S. Wilson, S. Gottesfeld, J. Appl. Electrochem. 22 (1992) 1–7.
[25] J.W. Kim, A.V. Virkar, K.Z. Fung, K. Mehta, S.C. Singhal, J. Electrochem. Soc. 146 (1999) 69–78.
[26] S.C. Singhal, K. Kendall, High-Temperature Solid Oxide Fuel Cells: Fundamentals, Design and Applications, Oxford, Elsevier, 2003.
[27] X.H. Deng, A. Petric, J. Power Sources 140 (2005) 297–303.
[28] S. Rey-Mermet, P. Muralt, Solid State Ionics 179 (2008) 1497–1500.
[29] P. Muralt, S. Rey-Mermet, Y. Yan, C. Sandu, G. Deng, Thin Solid Films 518 (2010) 4743–4746.
[30] S. Ramanathan, H. Xiong, B.K. Lai, A.C. Johnson, J. Power Sources 193 (2009) 589–592.
[31] C.M. Kleinlogel, L.J. Gauckler, J. Electroceram. 5 (2000) 231–243.
[32] A. Bogicevic, J. Stromquist, B.I. Lundqvist, Phys. Rev. B 57 (1998) R4289–R4292.
[33] A. Bieberle-Hütter, J.L. Rupp, A. Evans, H. Galinski, B. Scherrer, R. Tölke, L.J. Gauckler, European Fuel Cell Forum, 2008, p. B0701.
[34] R. O'Hayre, D.M. Barnett, F.B. Prinz, J. Electrochem. Soc. 152 (2005) A439–A444.
[35] G.M. Choi, J.H. Joo, Solid State Ionics 177 (2006) 1053–1057.
[36] A. Infortuna, A.S. Harvey, L.J. Gauckler, Adv. Funct. Mater. 18 (2008) 127–135.
[37] U.P. Muecke, D. Beckel, A. Bernard, A. Bieberle-Hutter, S. Graf, A. Infortuna, P. Muller, J.L.M. Rupp, J. Schneider, L.J. Gauckler, Adv. Funct. Mater. 18 (2008) 3158–3168.
[38] M.J. Jorgensen, M. Mogensen, J. Electrochem. Soc. 148 (2001) A433–A442.
[39] D. Beckel, U.P. Muecke, T. Gyger, G. Florey, A. Infortuna, L.J. Gauckler, Solid State Ionics 178 (2007) 407–415.
[40] C.R. Xia, F.L. Chen, M.L. Liu, Electrochem. Solid State 4 (2001) A52–A54.
[41] T. Yamaguchi, S. Shimizu, T. Suzuki, Y. Fujishiro, M. Awano, J. Electrochem. Soc. 155 (2008) B1141–B1144.
[42] B.K. Lai, K. Kerman, S. Ramanathan, J. Power Sources 195 (2010) 5185–5196.